Study of the ICRF Wave Coupling on ASDEX-Upgrade

S.-I Itoh*, K. Itoh**, A. Fukuyama+,
J.-M.Noterdaeme++, K. Steinmetz++, F. Wesner++

IPP 4/233 August 1987

MAX-PLANCK-INSTITUT FÜR PLASMAPHYSIK

8046 GARCHING BEI MÜNCHEN

MAX-PLANCK-INSTITUT FÜR PLASMAPHYSIK

GARCHING BEI MÜNCHEN

8/75

Study of the ICRF Wave Coupling on ASDEX-Upgrade

S.-I Itoh*, K. Itoh**, A. Fukuyama+,

J.-M.Noterdaeme++, K. Steinmetz++, F. Wesner++

IPP 4/233 August 1987

* Institute for Fusion Theory, Hiroshima University

** Plasma Physics Laboratory, Kyoto University

\+ School of Engineering, Okayama University

++ Max-Planck-Institut für Plasmaphysik

Die nachstehende Arbeit wurde im Rahmen des Vertrages zwischen dem Max-Planck-Institut für Plasmaphysik und der Europäischen Atomgemeinschaft über die Zusammenarbeit auf dem Gebiete der Plasmaphysik durchgeführt.

Abstract

ICRF (ion cyclotron range of frequencies) wave on the ASDEX-upgrade tokamak is studied theoretically. By applying a numerical code on the ICRF wave propagation to ASDEX-upgrade, the antenna coupling, wave accessibility and power deposition profile are calculated. The role of the scrape-off plasma on coupling is also discussed.

§ 1 Introduction

The use of ICRF (ion cyclotron range of frequencies) waves is now accepted as a dependable method for heating the plasma in large toroidal devices. The role of this heating method is becoming increasingly important for future machines.

Associated with the experimental progress of the ICRF wave heating experiments, the theoretical understanding on this heating has also deepened /1-4/. The excitation, propagation and absorption of the wave, as well as the fast particle generation and relaxation phenomena have been explained quantitatively. The analysis of the wave propagation, particularly, has made such a progress that we now have guidelines for the antenna design and the wave launching schemes. This has become possible by the development of a global wave analysis code /3,4/.

In this article we have applied our global wave calculation to ASDEX-Upgrade /5/ and study the characteristics of the ICRF wave propagation. The minority resonance heating and the second harmonic cyclotron resonance heating cases are investigated. Antenna loading, accessibility condition and power deposition profile are obtained. Attention is paid to the role of the plasma in scrape-off layer (SoL), in order to simulate the effect of the H/L transition on the ICRF coupling.

§ 2 Model and Basic Equation

We choose a simplified model geometry of ASDEX-Upgrade. For the first step of the analysis, a wave solution is obtained on the equatorial plane of the torus by taking a plasma slab model. In the model geometry, which is shown in Fig. 1, the $\hat{x}$-axis is taken in the direction of the major radius and $\hat{z}$-axis is in the toroidal direction. We assume that the slab is homogeneous in y- and z-directions.

The model distributions of the magnetic field, density and temperatures are chosen as

$$B_z(x) = B_o/[1+x/R], \tag{1}$$

$$n_j(x) = \begin{cases} (n_{jo} - n_{js})(1-x^2/a_s^2) + n_{js} & \text{for } |x| \leq a_s \\ n_{js}\exp\{-(|x|-a_s)/\lambda_n\} & \text{for } a_s \leq |x| \leq a_L \end{cases} \tag{2}$$

and

$$T_j(x) = \begin{cases} (T_{jo}-T_{js})(1-x^2/a_s^2) + T_{js} & \text{for } |x| \leq a_s \\ T_{js}\exp\{-(|x|-a_s)/\lambda_T\} & \text{for } a_s \leq |x| \leq a_L \end{cases} \tag{3}$$

where R is the major radius, a_s is the separatrix radius, a_L is the limiter radius, and the suffix j stands for the particle species. λ_n and λ_T are the fall-off length of density and temperature in the SoL plasma.

The Maxwell equation of the wave is written in the form as

$$\nabla\times\nabla\times \tilde{\vec{E}} + [1/c^2]\,[\partial^2/\partial t^2]\,\tilde{\vec{E}} = \mu_o\,\partial/\partial t(\sum_j \tilde{\vec{J}}_j + \tilde{\vec{J}}_{ext}) \tag{4}$$

where $\tilde{\vec{E}}$ is the electric field of the wave, $\tilde{\vec{J}}_j$ is the oscillating current carried by the j-species of the plasma and $\tilde{\vec{J}}_{ext}$ is the current on the antenna and wall. The explicit form of the rf conductivity, which is derived based on the kinetic theory, is shown in Refs. [3,4] and is not repeated here. The kinetic processes which are taken into account are: the finite gyroradius effect up to the second order, the fundamental and second harmonic cyclotron resonances, the Landau damping as well as the transit time magnetic pumping.

The boundary condition is given as

$$\frac{E_y'}{E_y} = \frac{E_z'}{E_z} = \mp \sqrt{k_z^2 - \frac{\omega^2}{c^2} - i\omega\mu_o \sigma_w} \qquad \text{at } x = \pm b \qquad (5)$$

on the wall, where ' denotes d/dx and σ_w is the conductivity of the wall material. The antenna is simulated to be a current carrying ribbon (with zero thickness), which has an arc length L_A and width in the toroidal direction L_T. The rf current on the antenna is in the y-direction and is given as

$$\tilde{\vec{J}}_A(\vec{r}, t) = \sum_{k_z} J_A(k_z)\, \delta(x-d) e^{i(k_z z - \omega t)}\, \hat{y} \qquad (6)$$

for the low-field side excitation. x = d indicates the radial location of the antenna. To simulate the width of the antenna, we simply choose

$$J_A(z) \propto \exp\{-4z^2/L_T^2\} \ . \qquad (7)$$

We first Fourier decompose eq. (4) and solve $\tilde{E}(x,k_z,\omega)$. Then the wave form on the equatorial plane $\tilde{E}(x,z,\omega)$ is obtained by the Fourier recomposition. The center of the antenna coincides with z = 0.

The absorbed power is calculated in two ways. Firstly, the power absorption to each species through the k_z-th component is given by

$$P_j(x;k_z) = \langle \tilde{J}_j(x;k_z)\, \tilde{E}(x;k_z) \rangle \tag{8}$$

where the symbol < > denotes the phase average. Integrating in the x-direction, the power to j-th species by the k_z-th component is given as

$$\bar{P}_j(k_z) = \int P_j(x,k_z)dx \tag{9}$$

The total power $\bar{P}(k_z)$ is given as

$$\bar{P}(k_z) = \Sigma_j \bar{P}_j \quad (j = e,i,w) \tag{10}$$

where j=w means the absorption on the wall. This quantity indicates how large a power is absorbed for given $\tilde{J}(k_z)$ and is a good measure to show the accessibility of the wave. The total absorption to the j-th species is defined as

$$\bar{P}_{jt} = \sum_{k_z} \bar{P}_j(k_z) \tag{11}$$

and the total absorption is similarly given as

$$\bar{P}_t = \sum_{k_z} \bar{P}(k_z) \tag{12}$$

The second way is to calculate the power deposition profile on the equatorial plane as

$$P_j(x,z) = \langle \tilde{J}_j(x,z) \cdot \tilde{E}(x,z) \rangle \tag{13}$$

The power deposition to j-th species by the global wave is given by integrating $P_j(x,z)$ as

$$\hat{P}(x) = \int P_j(x,z)dz \tag{14}$$

The total absorption profile, $\hat{P}_t$, is defined as

$$\hat{P}_t(x) = \Sigma_j \hat{P}_j(x) \tag{15}$$

This representation gives the spatial profile of the power absorption. The integral of $\hat{P}_t(x)$ in the x-direction agrees with $\bar{P}_t$.
The loading impedance $\hat{Z} = \hat{R}-i\hat{X}$ is defined by

$$\tilde{E} = \hat{Z}\tilde{I}_A \tag{16}$$

on the antenna ($\tilde{I} = \int \tilde{J}\, dz$). The loading resistance satisfies the relation

$$\bar{P}_t = 1/2\ \hat{R}\tilde{I}_A{}^2 \quad , \tag{17}$$

i.e., the energy conservation relation.

The method of the solution and accuracy of the solution are discussed in Refs. [3,4]. In the following calculation, we choose $\tilde{I}_A$ = 1 A unless specified to a particular value.

§ 3 Study on Minority Heating

The typical parameters are tabulated in the Table I. We study the case of majority deuteron and minority proton. The applied frequency is very close to the cyclotron frequency of protons at the plama center. For the plasma parameters, we choose the two reference cases given in Table II. The case A with the lower density and temperature simulates the target plasma of Ohmic discharge. The case B (higher density and temperature) is a model of the additionally heated plasma.

Figure 2 illustrates the power absorption spectrum $\bar{P}(k_z)$ for case A with n_H/n_e = 0.05. One notices a sequence of peaks which corresponds to the cavity mode. One general trend is that, at high parallel wave number, $\bar{P}(k_z)$ decay is quick. This is due to the evanescent region between the antenna and cut-off surface near the edge. One rough estimation of the accessible range is given as /6/ $|k_z| \lesssim k_{zc}$ where

$$k_{zc} \simeq \left(\frac{\omega_{pD}^2(0)}{c^2} \left| \frac{\Omega_D^2}{\omega^2 - \Omega_D^2} \right. \frac{n'_e(a_s)|}{n_e(0)} \right)^{1/3} \tag{18}$$

In this low-temperature plasma case, the total loading resistance is given as $\hat{R} \simeq$ 19 Ω/m. The power partition is as $\bar{P}_e : \bar{P}_D : \bar{P}_H$ = 0.05 : 0.1 : 0.85

The power deposition profile is given in Fig. 3 for this case. The deposition profile is peaked near the cyclotron resonance surface. As small amount of damping is seen in the peripheral region. This is due to the collisional absorption of the Bernstein wave.

When the density and temperature of the target plama increases, the wave coupling depends on the parameters more smoothly because of the improved absorption. Figure 4 illustrates the absorption spectrum for case B (model of additionally heated plasma). The ratio of the minority concentration is the same, $n_H/n_e = 0.05$. We see that the damping of the wave is strong and that the cavity resonances disappear. Figure 5 shows the wave structure for this case. The E_y component of the wave on the $z = 0$ plane is shown in Fig. 5(a). The wave is excited at the antenna and propagates to the plasma. Because of the good absorption, small amount of the wave tunnels to the high-field side. The standing wave component in the low-field side is also small. Figure 5(b) shows the power deposition profile. The contribution of deuterons becomes large because of the high temperature; the half width of the ion absorption profile also becomes wider. Direct absorption of the fast wave by electrons through Landau damping occurs. As compared to case A, we see that 1) the power deposition becomes wider and that 2) power partition changes:

$$\bar{P}_{et} : \bar{P}_{Dt} : \bar{P}_{Ht} \cong 0.29 : 0.28 : 0.43.$$

The wave form in vacuum is also shown in Fig. 5(c). The E_y component on the $x = d$ plane (where the antenna is located) shows that the wave field is localized within $\pm \pi/12$ in toroidal direction.

One concern is the effect of the density fall-off length. Associated with the H/L transition, the density fall-off length in the SoL changes rapidly. To study this effect we calculate $\hat{R}$ for various values of λ_n. The

value of λ_T is chosen to be equal to λ_n. Figure 6 shows the result. Because the loading resistance is high due to the setting of the antenna close to the plasma, the change of λ_n affects $\hat{R}$ strongly. As λ_n becomes larger, the cut-off surface comes closer to the antenna. The change of λ_n is more effective for the case B.

We finally see how the antenna width controls the loading impedance. The figure 7 illustrates $\hat{R}$ and $\hat{X}$ as a function of L_T. If the antenna width becomes narrow such as to satisfy $L_T\, k_{zc} \lesssim \pi$, the loading resistance saturates. For larger values of L_T, $\hat{R}$ scales as $1/L_T$. Because the large value of $\hat{R}$ and small value of $\hat{x}$ are favourable, the range of $0.15 \lesssim L_T \lesssim 0.2$ m is optimum for a single antenna width.

§ 4 The Second Harmonic Cyclotron Resonance Heating

The other fast wave heating scheme is the second harmonic cyclotron resonance heating. We study a case of with a pure hydrogen plasma and choose $\omega/2\pi$ = 80 MHz.

The absorption of the ICRF wave through the second cyclotron resonance is weak compared to the fundamental resonance in the minority scheme. Due to the weak damping, the cavity resonance effect becomes more prominent. Figure 8 illustrates the spectrum of the absorbed power for the case A. A train of sharp peaks appears. The half width of each peak is much sharper than that in Fig. 2. If the plasma pressure becomes high, the wave absorption is improved. The absorption spectrum $\bar{P}(k_z)$ is shown in Fig. 9 for the case B. The shape of $\bar{P}(k_z)$ become smooth as in the case of Fig. 4. The dotted line indicates the contribution of the electrons. In this case, $\bar{P}_e : \bar{P}_H = 0.19 : 0.81$ and about 20 % is absorbed by electrons directly. The total loading resistance is about 23 Ω/m. Compared to the low frequency case, the impedance becomes approximately twice as large.

One example of the power absorption profile is given in Fig. 10. $\hat{P}_H$ (solid line), $\hat{P}_e$ (dashed line) and $-\int S_x dz$ (dashed-dotted line : Poynting flux) are shown. The resonance absorption by the protons gives a sharp profile, while the absorption by the electrons takes place in the wide region of the plasma radius. The wave structure in the vacuum is shown in Fig. 11. The E_y component on the x=d plane is shown. The wave is localized in the toroidal direction due to the good coupling. As is shown by Eq. (18), the higher k_z modes are in cut-off. One evaluation of the width of the wave envelope in the toroidal direction is given by $2\pi/k_{zc}$.

Figure 12 shows the effect of the density fall-off length. $\hat{R}$ and $\bar{P}_{et}$ are shown. As in the case of the minority heating scheme $\hat{R}$ becomes small if one reduces λ_n. Parameters are those of the case B. If one increases λ_n, then the cut-off surface approches to the limiter radius. If the density at $x = q_L$ becomes high enough then the cut-off surface does not move associated with the increment of λ_n. It is also noted that the relative contribution of $\bar{P}_{et}$ to $\bar{P}_t$ becomes larger for the larger values of λ_n. This is because the increment of λ_n improves the accessibility of the larger k_z modes which are more easily absorbed by electrons. For the case of a high temperature target plasma, the condition $2k_{\parallel} v_e \gtrsim \omega$ is satisfied at the plasma center for the components of $k_{\parallel}R \gtrsim 14$. Figure 13 shows the power absorption spectrum for the cases of λ_n = 0.5, 1.5, 3 cm. As the density fall-off length becomes larger, the absorption of the higher-k_z components are improved.

Before closing this section, we briefly discuss the effect of the control of the phase between two antennae. We consider a pair of two antennae (L_T = 15 cm for each and the interval between them is 15 cm). As is seen from Fig. 11, the wave localization length in the toroidal direction is longer than the distance between the two antenna, so interference between two antennae is expected, and the loading is controlled by the phasing. The distribution of the current on each antenna is chosen to be the same as Eq. (7) (translated in the z-direction). We study the in-phase case (I_A = 1 A for the both antenna) and the out-phase case (I_A = 1 A in one antenna and I_A = -1A in the other antenna). The loading resistance (per unit length) of each antenna $\hat{R}$ is defined as

$$\hat{R} = \bar{P}_t \qquad (19)$$

following eq. (18). In the absence of the interference, $\hat{R}$ reduces to the value of the single antenna.

By choosing the phasing, we can shift the peak of the spectrum of the excited wave. In the case of the out-phase, peak of $J_A(k_z)$ is located around $k_z R \simeq 18$. If $\bar{P}_t(k_z)/J_A^2(k_z)$ has a peak not at $k_z R \simeq 0$, then the out of phase case can have a larger loading resistance. In Fig. 12, we show the case of the in-phase and out-of phase. As is understood from Fig. 13, the out-of phase increases the loading, while the loading resistance reduces in the in-phase case. It is noted that the λ_n dependence of $\hat{R}$ is weak in the in-phase case. This would be advantageous to keep a stable loading in the case of the L/H transition.

§ 5 Summary

In this article, we study the ICRF wave excitation/propagation in the ASDEX-Upgrade tokamak. Based on the global wave calculation, the accessibility condition, antenna loading, power deposition and partition of the direct power absorption are obtained.

The wave coupling is good if the antenna location is as close to the plasma as is shown in Table I. The choice of the antenna parameter, such as the width, is in the range of the optimum condition from the view point of the coupling.

The study on the effect of the density fall-off length shows that the antenna loading is sensitive to λ_n. In the absence of the SoL plasma, $\hat{R}$ may be reduced to 70 % of that in the case of λ_n = 2 cm. This lower bound of the loading resistance seems high enough for the high power injection of the MW level. From this point of view, the control of the phasing between two antennae is of importance for experimental flexibility. By choosing a proper phasing, the sudden change of $\hat{R}$ associated with L/H transition can be reduced.

Acknowledgements

Two of the authors (S.I.I. and K.I.) acknowledge Drs. F. Wagner and H. Wobig for their hospitality during their stay in Max-Planck-Institute für Plamaphysik. Support from Mr. J. Kisslinger and Mrs. I. Ott on running computer codes and discussions with Dr. M. Brambilla are also acknowledged.

References

/1/ Stix, T.H., Nucl. Fusion 15 (1975) 739

/2/ Adam, J., Plasma Physics and Controlled Fusion 29 (1987) 443

/3/ Fukuyama, A., Nishiyama, S., Itoh, K., Itoh, S.-I., Nucl. Fusion 23 (1983) 1005

/4/ Fukuyama, A., Itoh, K., Itoh, S.-I., Computer Physics Reports 4 (1986) 139

/5/ a) ASDEX-Upgrade additional heating, IPP Report 1/237, Max-Planck-Institut for Plasmaphysics, Garching, April 1985

b) Söll, M., Noterdaeme, J.-M., Controlled Fusion and Plasma Heating, Europhysics Conf. Abstracts. Vol. 3F, Part 2, p. 100

c) Wesner, F., Noterdaeme, J.-M., Controlled Fusion and Plasma Heating, Europhysics Conf. Abstracts, Vol. 10 C, Part 2, p. 173

/6/ Itoh, K., Itoh, S.-I., Fukuyama, A., Nucl. Fusion 24 (1984) 13.

Table I

Main magnetic field	$B = 2.7$ T
Major radius	$R = 1.65$ m
Minor radius	$a_s = 0.5$ m (separatrix)
limiter radius	$a_L = 0.53$ m
Antenna radius	$d = 0.55$ m (low field side)
Wall radius	$b = 0.65$ m
Antenna arc length	$L_A = 1.1$ m
Antenna width	$L_T = 0.14$ m
Applied frequency	$\omega/2\pi = 40$ MHz (two-ion hybrid resonance heating)
	= 80 MHz (second cyclotron resonance heating)
Density fall-off length	$\lambda_n = 0.02$ m
Temperatur fall-off length	$\lambda_T = 0.02$ m.

Table II

		case A	case B
n_{eo}	≃	10^{20} m^{-3}	2 x 10^{20} m^{-3}
n_{es}		3 x 10^{19} m^{-3}	5 x 10^{19} m^{-3}
T_{eo}		1 keV	5 keV
T_{io}		1 keV	5 keV
T_{es}		50 eV	0.1 keV
T_{is}		50 eV	0.1 keV
n_H/n_e	≃	5 % (two ion hybrid resonance)	5 %
	≃	100 % (pure second harmonics)	100 %

Figure Captions

Fig. 1 Illustration of the model geometry.

Fig. 2 Spectrum of the coupled power vs $k_z R$ for the minority heating. Parameters are: $n_e(0) = 10^{20}/m^3$, $n_e(a_s) = 3 \times 10^{19}$ m^3, $T_{eo} = T_{io} = 1$ keV, $T_{es} = T_{is} = 50$ eV, $n_H/n_e = 5$ %, $\lambda_n = \lambda_T = 2$ cm, $\omega/2\pi = 40$ MHz. Other parameters are the same as in Table I. Partition between e, D and H are: $\bar{P}_t : \bar{P}_D : \bar{P}_H$ = 0.048 : 0.104 : 0.848.

Fig. 3 Power deposition profile for the case of Fig. 2. Solid line shows $\hat{P}(x)$ and the dashed line indicates the Poynting flux, $-\int S_x(x,z)dz$. Small dip on $\hat{P}_{tot}$ at $x \simeq 0.1$ a is due to the node of the wave. Peripheral damping is due to collisional absorption of the Bernstein wave by electrons.

Fig. 4 Power absorption spectrum for the case of minority heating on a hot and dense target plasma. $n_e(0) = 2 \times 10^{20}$ m^{-3}, $T_{eo} = T_{io} = 5$ keV, $n_s = 10^{20}$ m^{-3} and $T_s = 0.1$ keV. Other parameters are the same as in Fig. 2. The dotted-dashed line, the dotted line, and broken line indicate $\bar{P}_H$, $\bar{P}_D$, $\bar{P}_e$, respectively. Also illustrated is the relative amplitude of $\tilde{J}_A^2(k_z)$.

Fig. 5 Wave form and power deposition in the case of Fig. 4. The E_y component on z=0 plane, the power deposition profiles $\hat{P}(x)$ (for H, D and e) are shown as functions of x in (a) and (b). Part (c) shows the E_y component on the x=d plane. The wave in the vacuum is localized within $\pm \pi/8$ in toroidal angle near the antenna. Due to the strong damping, the wave form is close to the plane wave, with small cavity formation. The corrugations on $\hat{P}$ indicate the existence of a small amount of reflected wave component.

Fig. 6 Dependence of the loading resistance on the fall-off length of the scrape-off plasma. Dashed line is a low-density case (Fig. 2) and solid line is a case of high density (Fig. 5). In the case of low edge density n_s, the effect of λ_n seems weak. We here notice that this weak dependence is due to the presence of the cavity eigenmode, the Q-value of which is over estimated in the one-dimensional approximation: the reduction of $\hat{R}$ for smaller value of λ_n may be underestimated by the 1D model in the case of low edge density.

Fig. 7 Dependence of the antenna impedance on the antenna width. Parameters are chosen as those in Fig. 2.

Fig. 8 Power absorption spectrum in the case of the second cyclotron heating of pure hydrogen plasma. $\omega/2\pi$ = 80 MHz, $n_H = n_e$ and other parameters are the same as those in Fig. 2.

Fig. 9 Power absorption spectrum for the case of the high density and high temperature target plasma (second cyclotron heating of H-plasma). Plasma parameters are the same as in Fig. 4, except $n_H = n_e$ in this case. $\omega/2\pi$ = 80 MHz. The partition of the power absorption in $\bar{P}_e : \bar{P}_H = 0.19 : 0.81$.

Fig. 10 Power deposition profile for the case of Fig. 9.

Fig. 11 The electric field on the plane x = d. The fast wave component is localized in the vicinity of the antenna within the toroidal angle of $\pm \pi/12$.

Fig. 12 Dependence of the loading resistance on λ_n for the second cyclotron resonance heating (solid line). The dotted line indicate the power absorbed by electrons. Other parameters are the same as in Fig. 9. The dashed line and dotted-dashed line are for the case of in-phase (0,0) and out-phase $(0,\pi)$ operation of a pair of two antennae (loading resistance of each antenna is shown). By controlling the phase, one can either enhance the resistance or reduce the λ_n dependence of $\hat{R}$.

Fig. 13 The spectrum of the absorption profile for various values of λ_n (λ_n = 0.5, 1.5, 3 cm). As λ_n increases, the accessibility of the modes with larger k_z is improved. As a result of it, the electron absorption increases. Other parameters are the same as in Fig. 9.

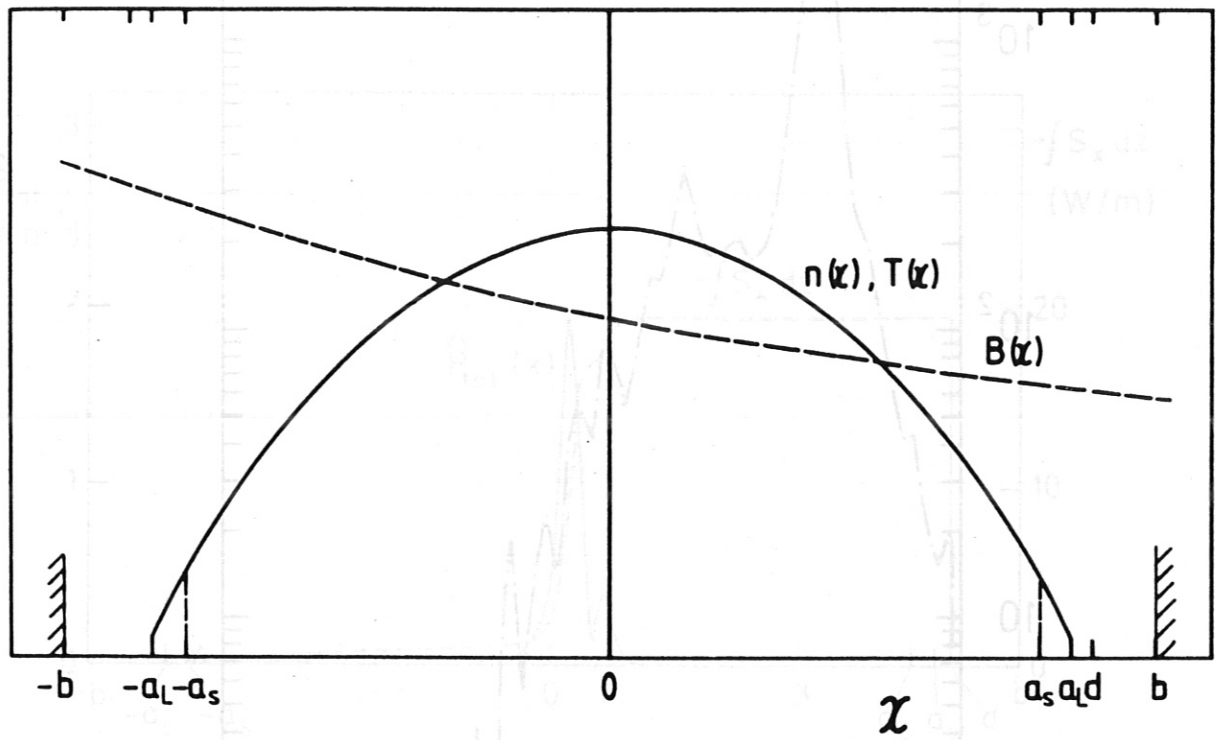

Fig. 1 Illustration of the model geometry.

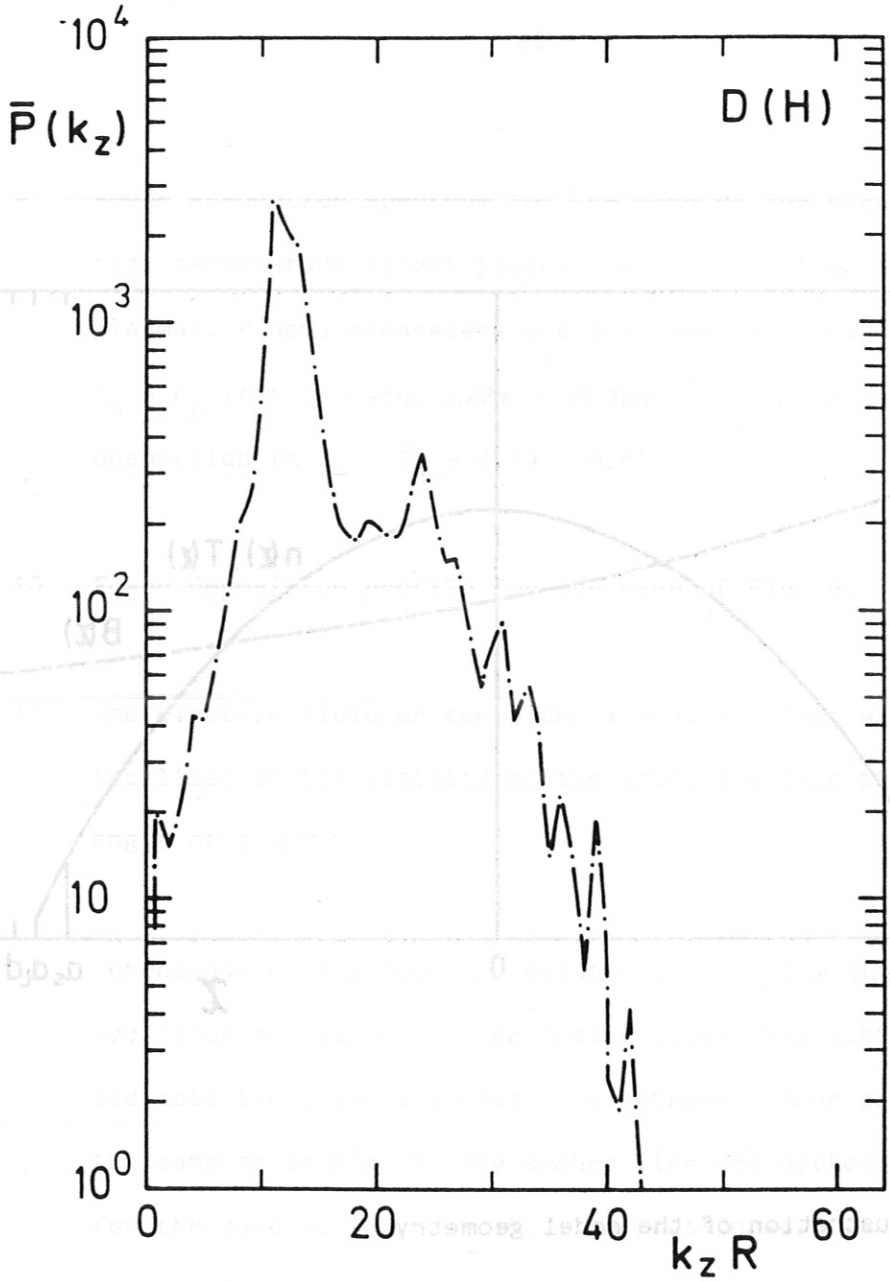

Fig. 2 Spectrum of the coupled power vs $k_z R$ for the minority heating. Parameters are: $n_e(0) = 10^{20}/m^3$, $n_e(a_s) = 3 \times 10^{19}/m^3$, $T_{eo} = T_{io} = 1$ keV, $T_{es} = T_{is} = 50$ eV, $n_H/n_e = 5$ %, $\lambda_n = \lambda_T = 2$ cm, $\omega/2\pi = 40$ MHz. Other parameters are the same as in Table I. Partition between e, D and H are: $\bar{P}_t : \bar{P}_D : \bar{P}_H = 0.048 : 0.104 : 0.848$.

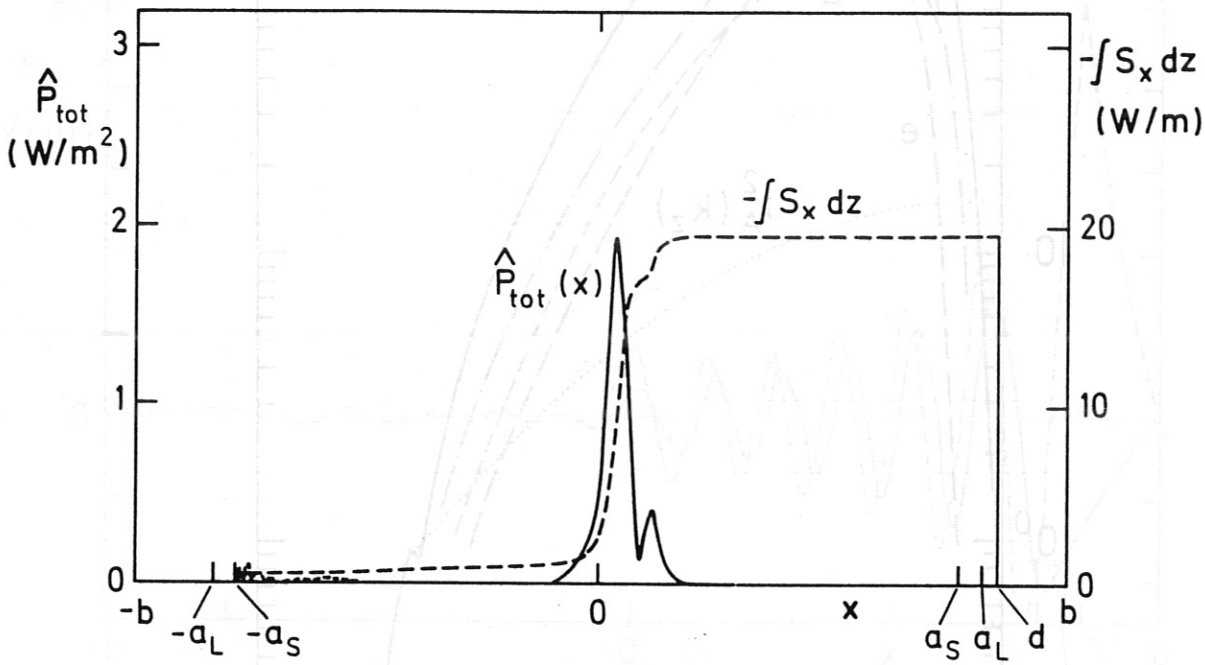

Fig. 3 Power deposition profile for the case of Fig. 2. Solid line shows $\hat{P}(x)$ and the dashed line indicates the Poynting flux, $-\int S_x(x,z)dz$. Small dip on $\hat{P}_{tot}$ at $x \simeq 0.1$ a is due to the node of the wave. Peripheral damping is due to collisional absorption of the Bernstein wave by electrons.

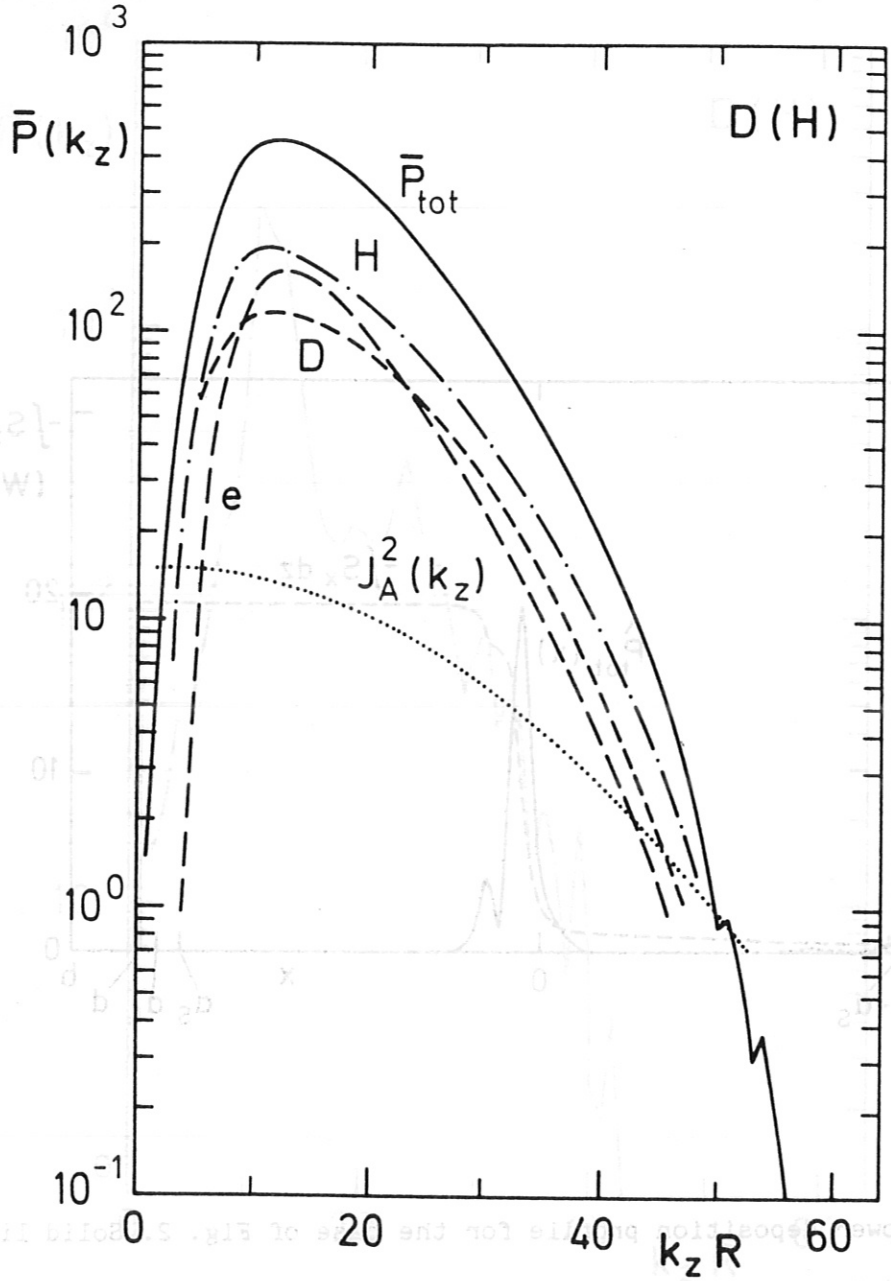

Fig. 4 Power absorption spectrum for the case of minority heating on a hot and dense target plasma. $n_e(0) = 2 \times 10^{20}$ m^{-3}, $T_{eo} = T_{io} = 5$ keV, $n_s = 10^{20}$ m^{-3} and $T_s = 0.1$ keV. Other parameters are the same as in Fig. 2. The dotted-dashed line, the dotted line, and broken line indicate $\bar{P}_H$, $\bar{P}_D$, $\bar{P}_e$, respectively. Also illustrated is the relative amplitude of $\tilde{J}_A^2(k_z)$.

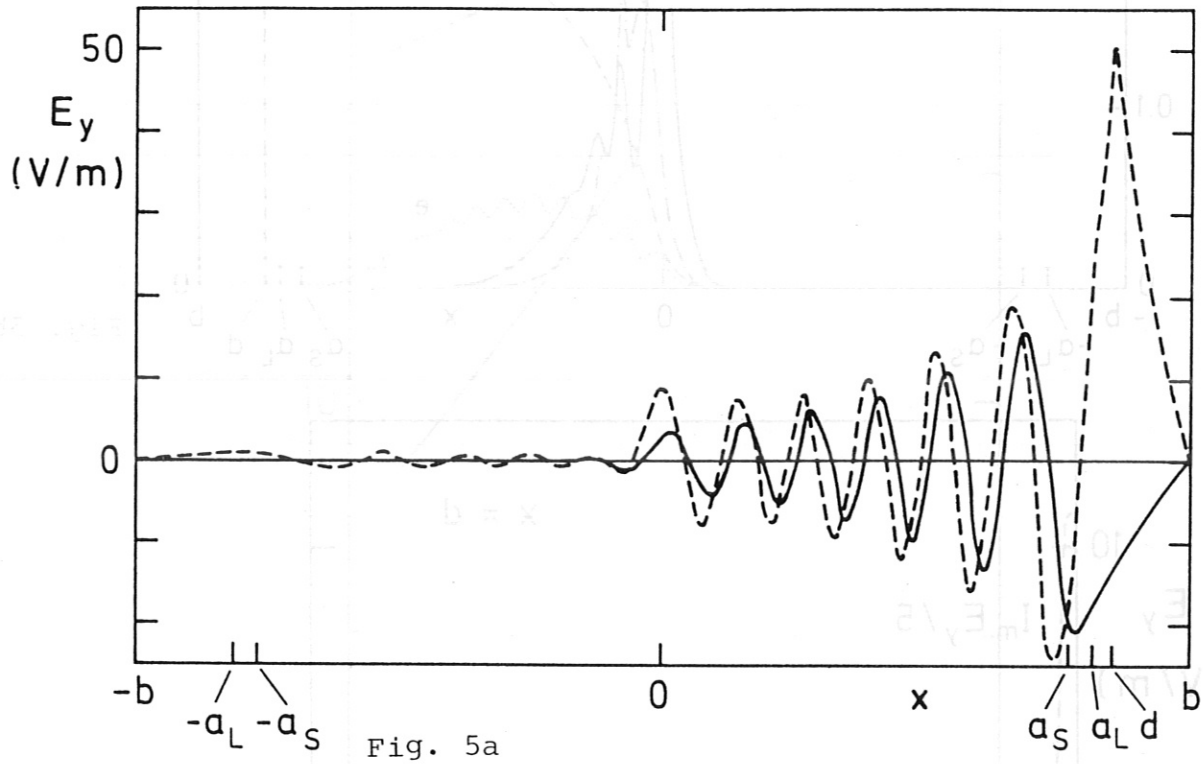

Fig. 5a

Fig. 5 Wave form and power deposition in the case of Fig. 4. The E_y component on z=0 plane, the power deposition profiles $\hat{P}(x)$ (for H, D and e) are shown as functions of x in (a) and (b). Part (c) shows the E_y component on the x=d plane. The wave in the vacuum is localized within $\pm \pi/8$ in toroidal angle near the antenna. Due to the strong damping, the wave form is close to the plane wave, with small cavity formation. The corrugations on $\hat{P}$ indicate the existence of a small amount of reflected wave component.

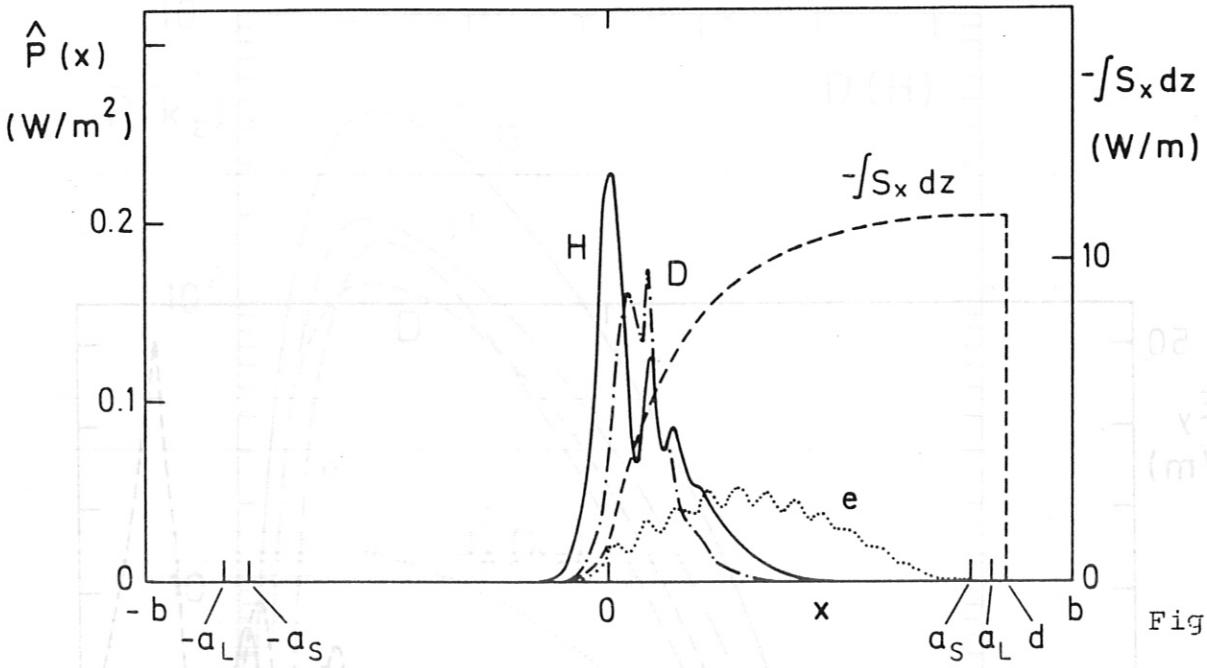
$\hat{P}(x)$
(W/m²)
0.2
0.1
0
H
D
e
$-\int S_x\,dz$
$-\int S_x\,dz$
(W/m)
10
0
- b
$-a_L$
$-a_S$
0
x
a_S
a_L
d
b

Fig. 5b

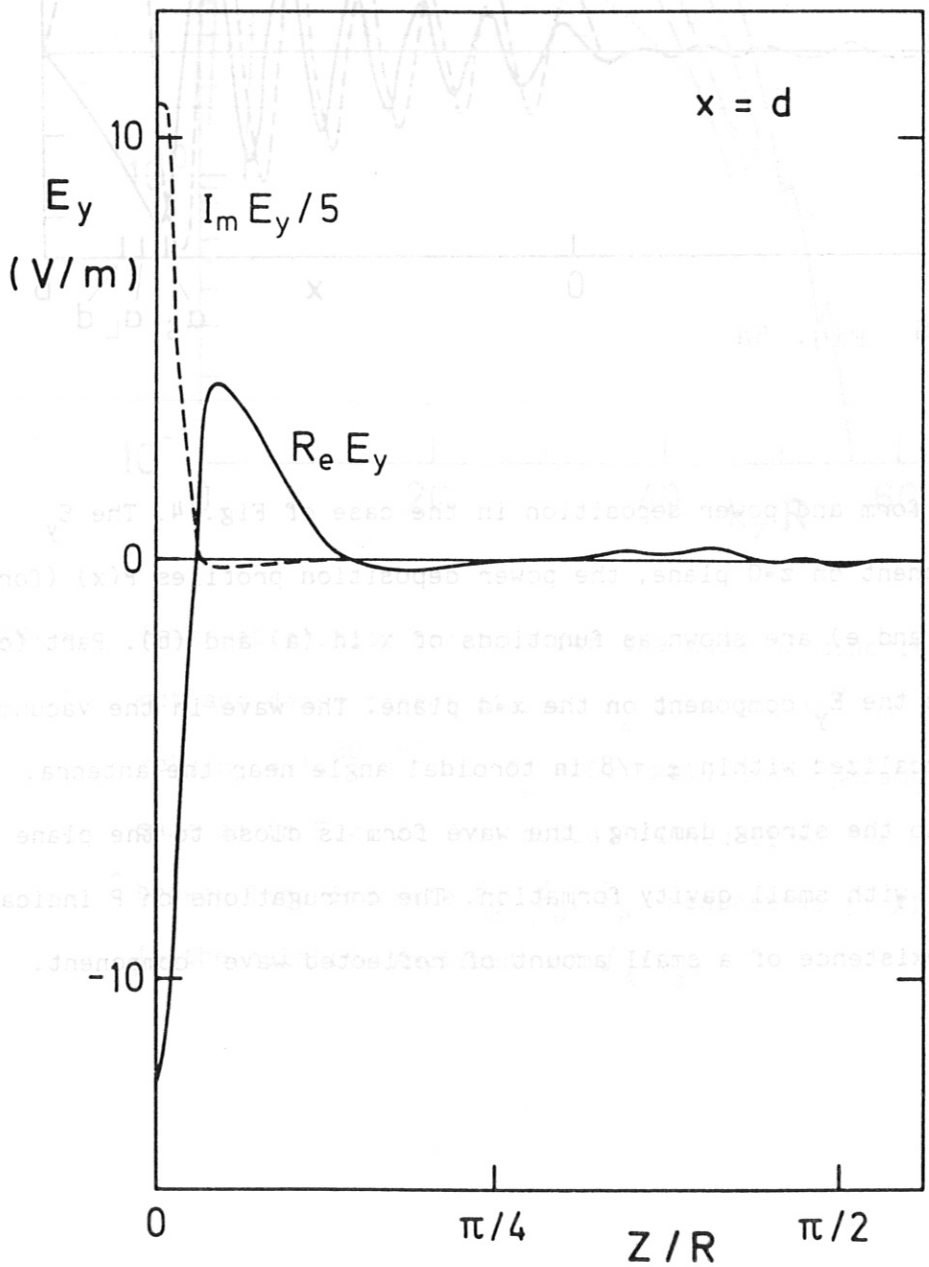
x = d
10
E_y
(V/m)
$I_m E_y/5$
$R_e E_y$
0
-10
0
π/4
π/2
Z/R

Fig. 5c

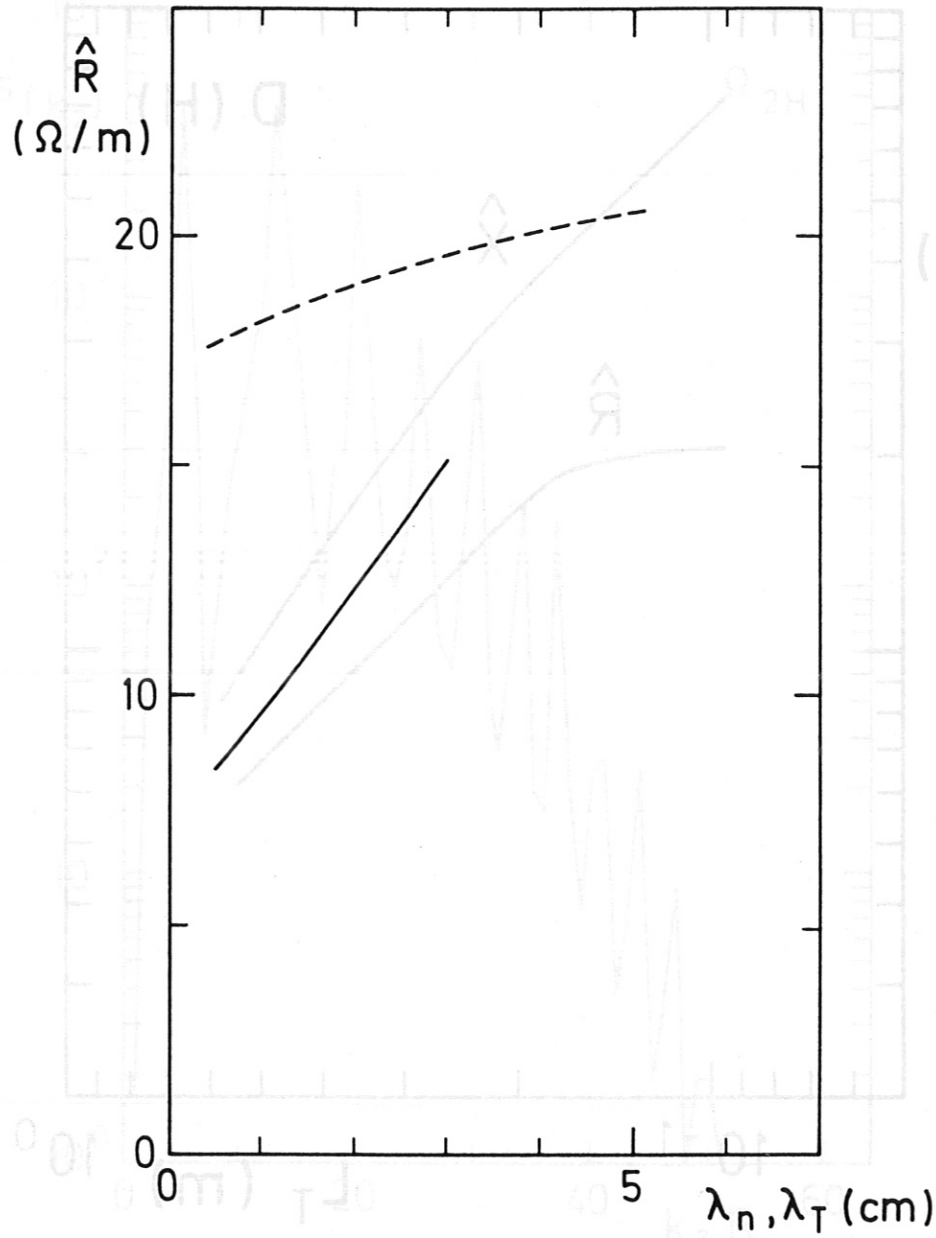

Fig. 6 Dependence of the loading resistance on the fall-off length of the scrape-off plasma. Dashed line is a low-density case (Fig. 2) and solid line is a case of high density (Fig. 5). In the case of low edge density n_s, the effect of λ_n seems weak. We here notice that this weak dependence is due to the presence of the cavity eigenmode, the Q-value of which is over estimated in the one-dimensional approximation: the reduction of $\hat{R}$ for smaller value of λ_n may be underestimated by the 1D model in the case of low edge density.

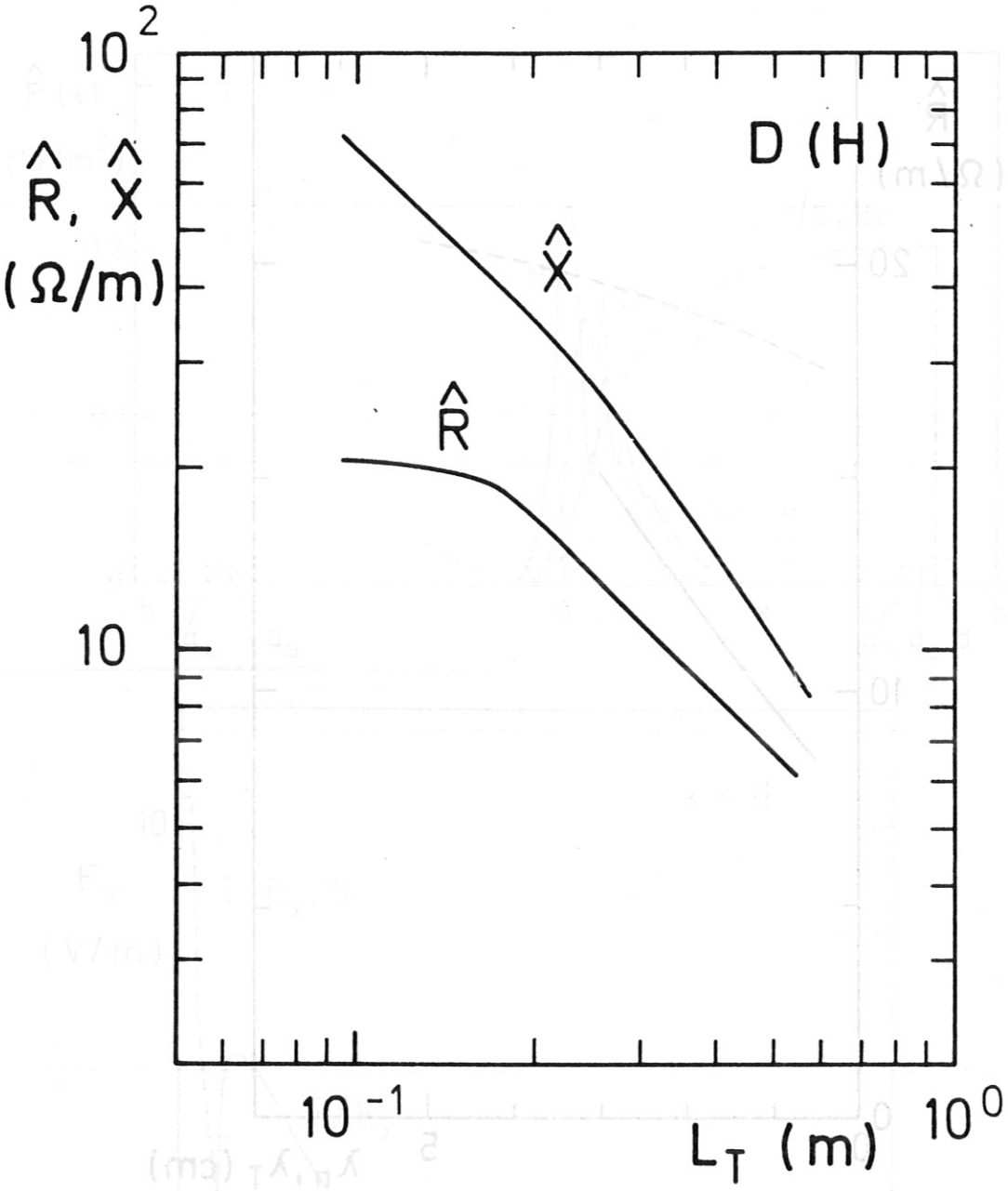

Fig. 7 Dependence of the antenna impedance on the antenna width. Parameters are chosen as those in Fig. 2.

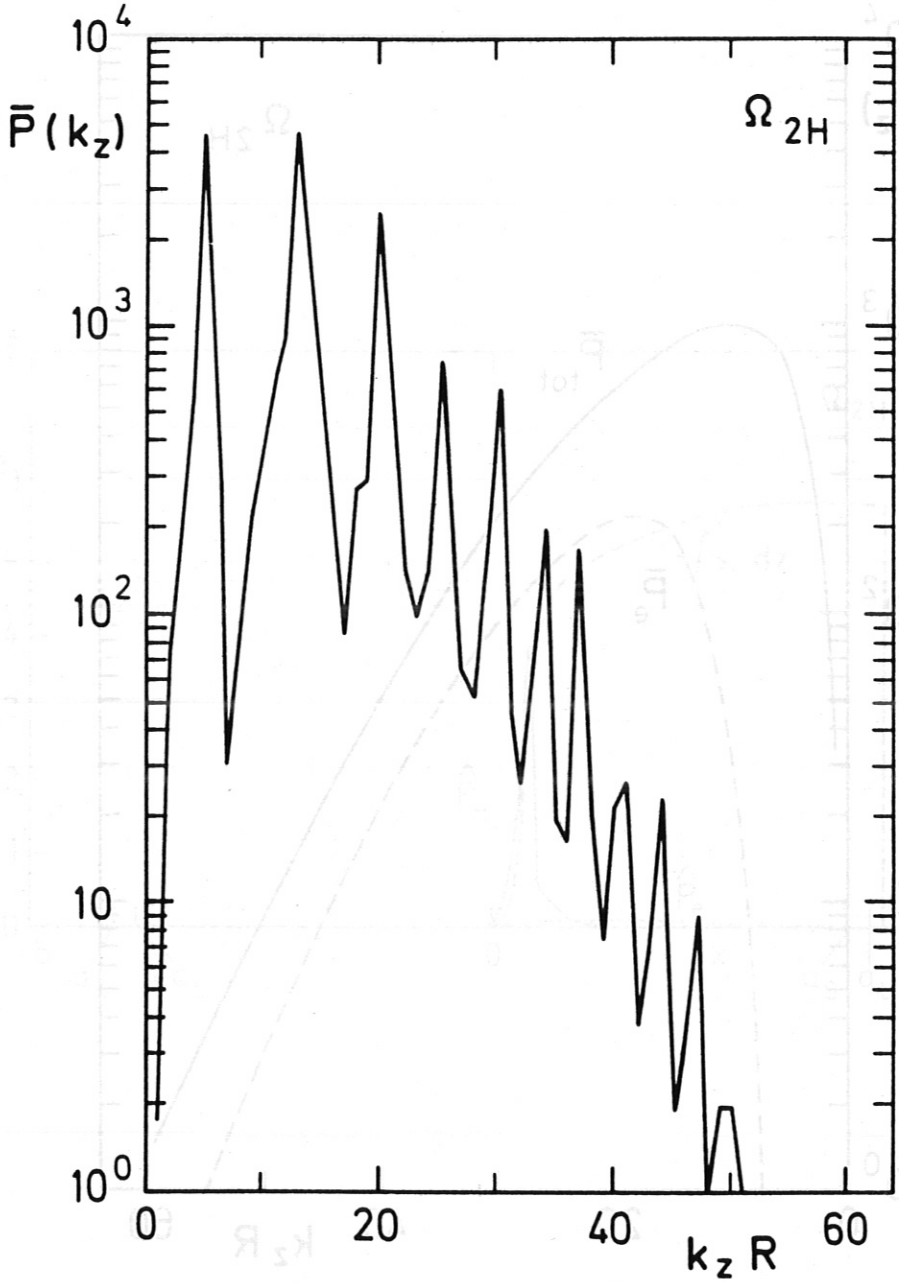

Fig. 8 Power absorption spectrum in the case of the second cyclotron heating of pure hydrogen plasma. $\omega/2\pi$ = 80 MHz, $n_H = n_e$ and other parameters are the same as those in Fig. 2.

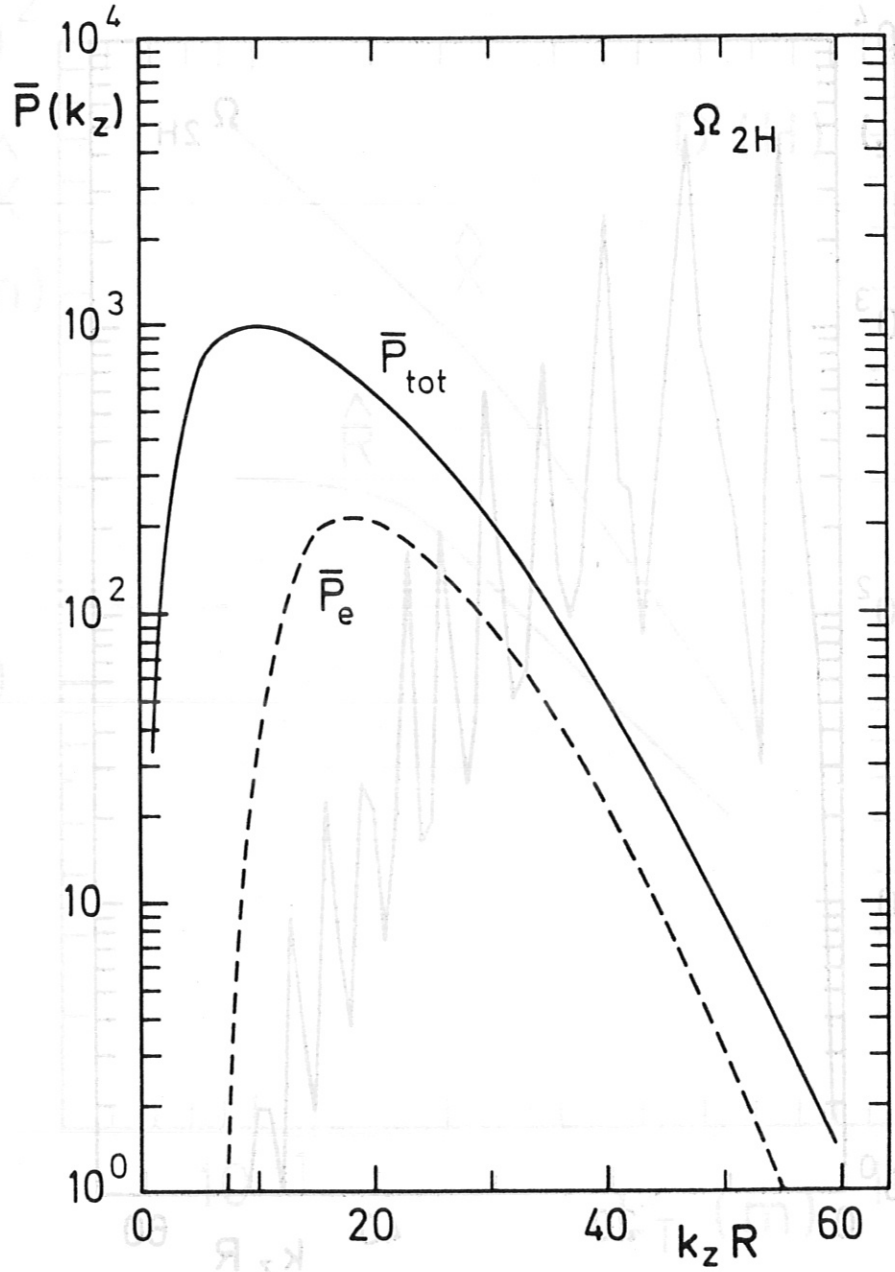

Fig. 9 Power absorption spectrum for the case of the high density and high temperature target plasma (second cyclotron heating of H-plasma). Plasma parameters are the same as in Fig. 4, except $n_H = n_e$ in this case. $\omega/2\pi$ = 80 MHz. The partition of the power absorption in $\bar{P}_e : \bar{P}_H$ = 0.19 : 0.81.

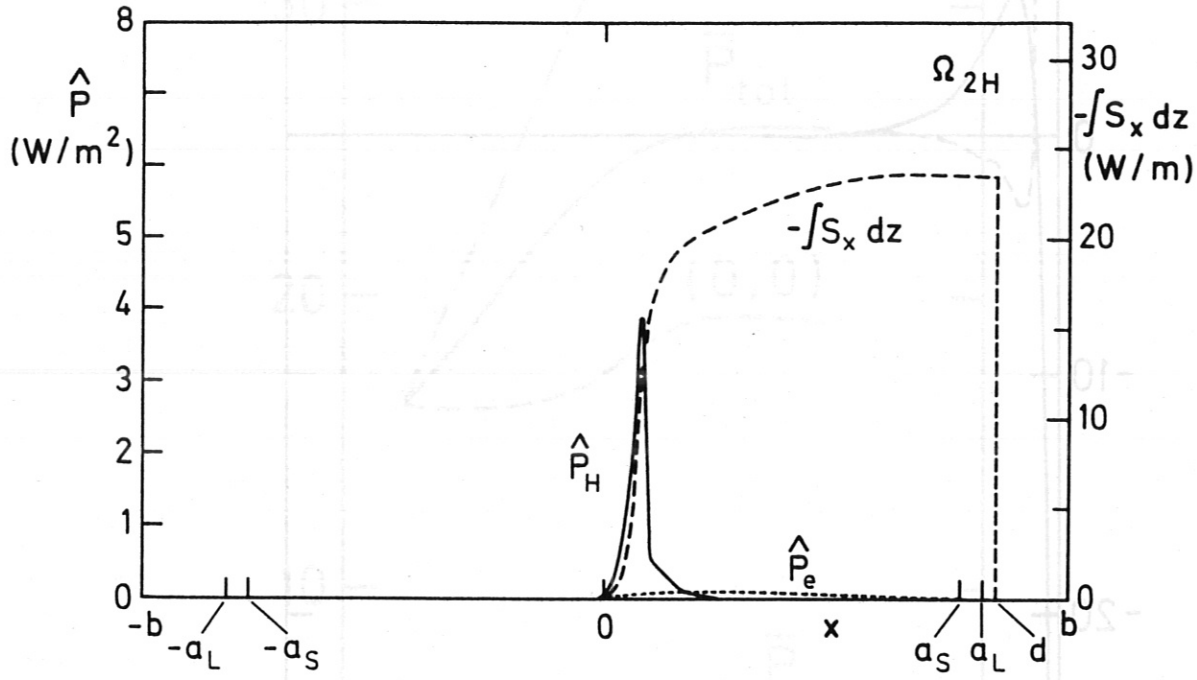

Fig. 10 Power deposition profile for the case of Fig. 9.

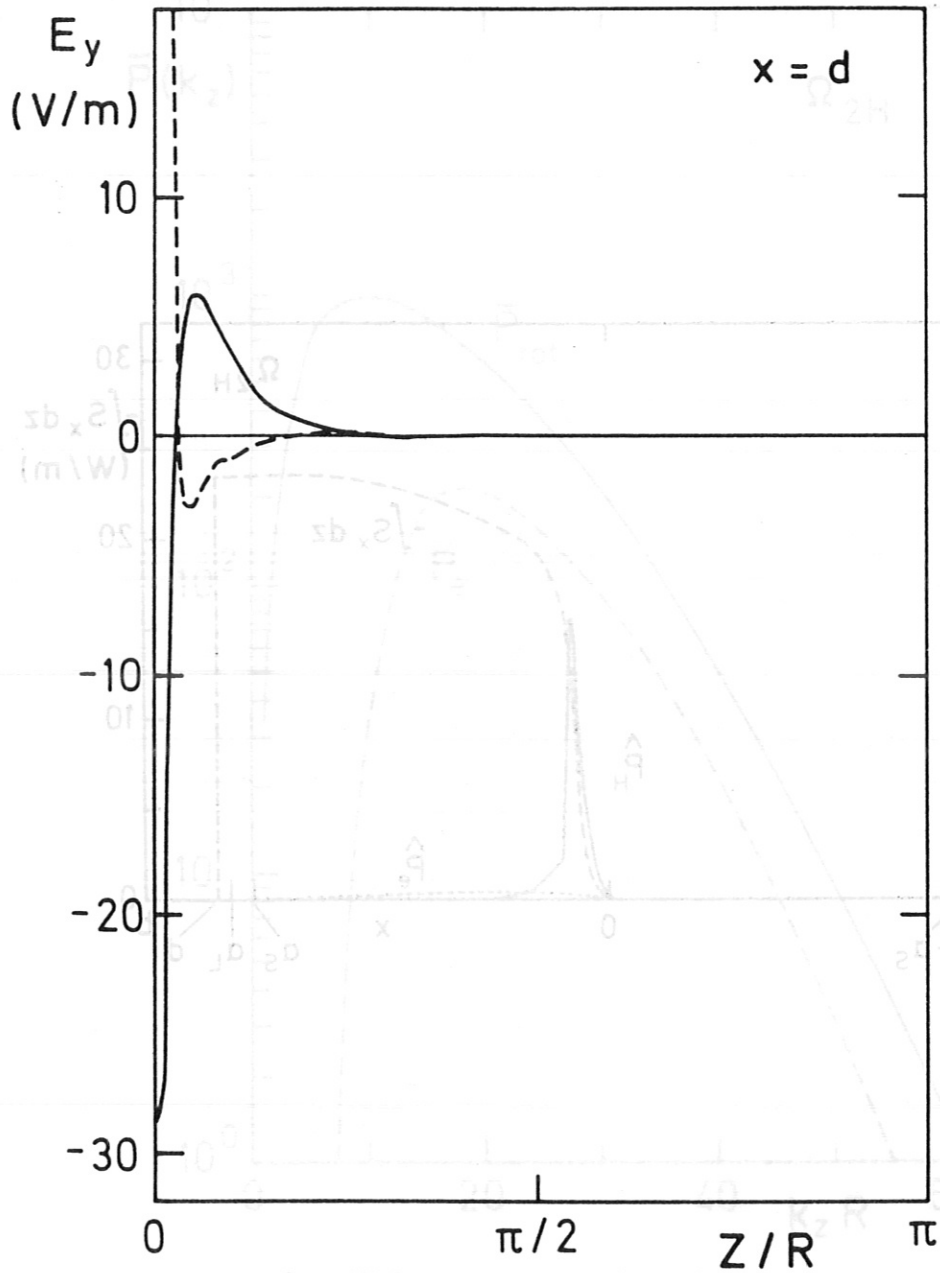

Fig. 11 The electric field on the plane x = d. The fast wave component is localized in the vicinity of the antenna within the toroidal angle of ± π/12.

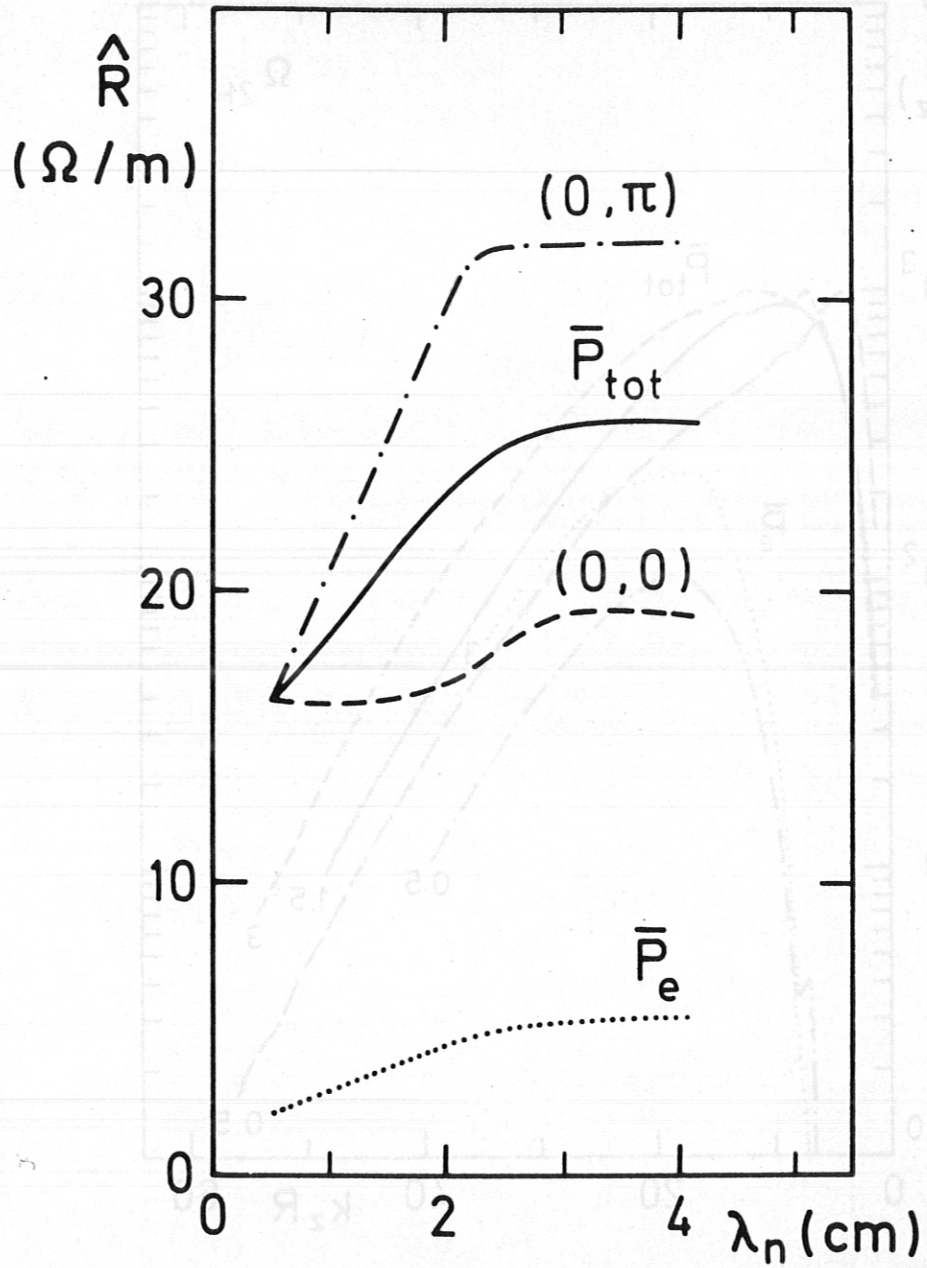

Fig. 12 Dependence of the loading resistance on λ_n for the second cyclotron resonance heating (solid line). The dotted line indicate the power absorbed by electrons. Other parameters are the same as in Fig. 9. The dashed line and dotted-dashed line are for the case of in-phase (0,0) and out-phase (0,π) operation of a pair of two antennae (loading resistance of each antenna is shown). By controlling the phase, one can either enhance the resistance or reduce the λ_n dependence of $\hat{R}$.

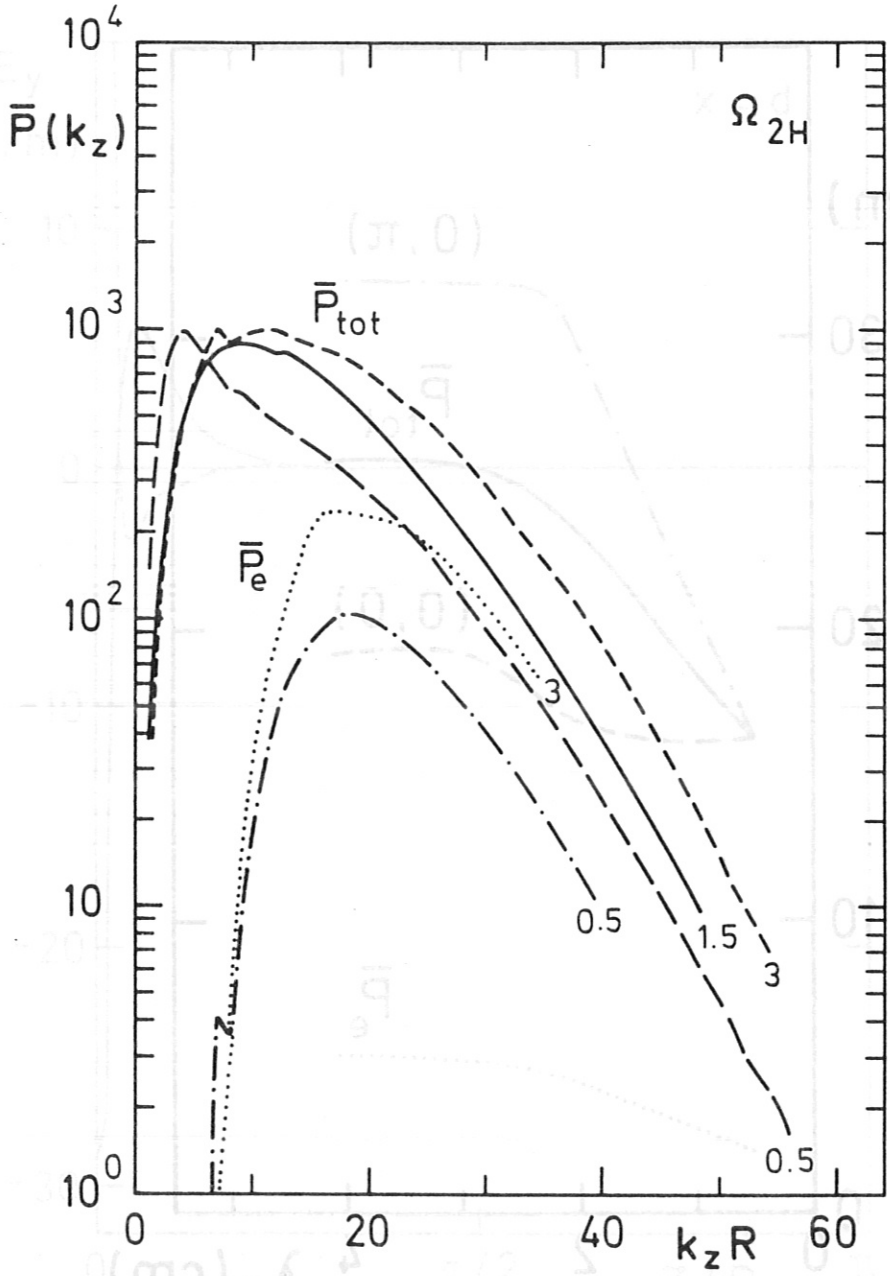

Fig. 13 The spectrum of the absorption profile for various values of λ_n (λ_n = 0.5, 1.5, 3 cm). As λ_n increases, the accessibility of the modes with larger k_z is improved. As a result of it, the electron absorption increases. Other parameters are the same as in Fig. 9.